Oxide-free InP-on-Silicon-on-Insulator Nanopatterned Waveguides: Propagation Losses Assessment Through End-Fire and Internal Probe Measurements

C. Pang, Henri Benisty, Mondher Besbes, Xavier Pommarede, Anne Talneau

Oxide-free InP-on-Silicon-on-Insulator Nanopatterned Waveguides: Propagation Losses Assessment Through End-Fire and Internal Probe Measurements

C.Pang, H.Benisty, M.Besbes, X.Pommarede, and A.Talneau

***Abstract*—Directly bonded, oxide-free, InP-based epitaxial layer bonding onto nanopatterned silicon-on-insulator structures was performed and result in waveguides with an embedded effective medium. Such a medium ensures flexible form of optical confinement and could also assist heat and electric current transfer optimally to the silicon layer since there is a remarkable absence of oxide, thanks to careful surface preparation processes. The fabricated waveguides, which embed buried 1-D (trenches) or 2-D (holes forming a photonic crystal) nanopatterns have been measured by two techniques. Either the classical end-fire technique, or the "internal light source" technique used for III–V-based photonic crystal waveguides, with a layer that contains several quantum wells. Propagation losses due to scattering in the nanopatterned area are retrieved by both methods and consistently point toward a $\sim$20 cm^{-1} loss level. A critical assessment is made of this result. Other local probe techniques allowed by the internal probe methods are reported that could help qualifying thermal transfer at these oxide-free interfaces.**

***Index Terms*—Hybrid integrated circuit bonding, integrated optoelectronics, photoluminescence (PL), waveguides.**

I. Introduction

SILICON photonics has become a major driver of photonic integration. Photonic integrated circuits (PIC) that exploit silicon-on-insulator (SOI) are increasingly functional. The elaboration of laser sources intimately based on SOI technology has been fueled by the advent of "hybrid evanescent silicon lasers" in 2006 [1]–[5]. The crucial assembly technology step is the bonding or wafer fusion of the InP-based stack to the patterned silicon chip [6], even though the photonic design efforts around this step are of high importance [7], [8]. In all the processes reported, InP is not directly in atomic contact. This is obvious in polymer-based bonding (the common process uses "DVS-BCB", see [2]). This is also clear for thick SiO_2 layers [5], [8]. For Bower's team processes, a very thin oxide layer of 5 nm or a single plasma activation is typically involved. It is of course nonetheless an electrical barrier, and is thermally equivalent to about 400 nm of silicon given the low thermal conductivity of silica. In the case of 300 °C bonding in ambient air, with oxide-free preparation [4], [9], a thin oxide amorphous layer is produced at the GaAs–Si interface.

Recent contributions on heteroepitaxial bonding have demonstrated oxide-free InP/Si interface with an atomic scale reconstructed interface thanks to oxide-free surface preparation and oxide-free annealing conditions [10], [11]. Such a *bona fide* InP/Si interface should permit high electrical performance similar to standard epitaxial layers.

Here, we bring this capability one step closer to the realization of actual PIC with such high-performance oxide-free bonding: we elaborated monomode channel waveguides by bonding InP-based layers that are made of pure InP or that contain active luminescent quantum wells (QWs) to a nanopatterned SOI substrate. We thus take advantage of the new bonding technology to revisit the spirit of hybrid lasers: if heat (and electrical current) fluxes can be efficiently channeled across the interface, novel designs can be made that simultaneously optimize thermal and optical performances for instance [12], mainly thanks to nanopatterned lateral cladding around ridge channel waveguides in the silicon part of the waveguide.

This paper reports the investigation of such waveguides as follows: In Secion II, samples are briefly described. In Section III, internal light source (ILS) measurement using photoluminescence (PL) are reported, and their analysis to provide the excess loss due to scattering by the nanopatterned cladding is discussed. In Section IV, results on end-fire measurements of similar waveguides are reported. Section V is devoted to a discussion. In Section VI, we describe as a complement how a local probe of embedded nanostructures can be assessed by band-filling studies with the micro-PL set-up used for ILS measurement. We then conclude in Section VII.

II. Sample Description

The samples studied here were obtained as follows: a SOI wafer with a $\sim$410 nm Si layer above a 1.56-μm-thick oxide layer was first patterned with the two kinds of geometries

C. Pang, H. Benisty, and M. Besbes are with the Laboratoire Charles Fabry, Institut d'Optique, CNRS, Univ Paris Sud, 91127 Palaiseau cedex, France (e-mail: chengxin.pang@gmail.com; henri.benisty@institutoptique.fr; mondher.besbes@institutoptique.fr).

A. Talneau and X. Pommarède are with the Laboratoire de Photonique et de Nanostructures, CNRS, F-91460 Marcoussis, France (e-mail: anne.talneau@lpn.cnrs.fr; xavier.pommarede@lpn.cnrs.fr).

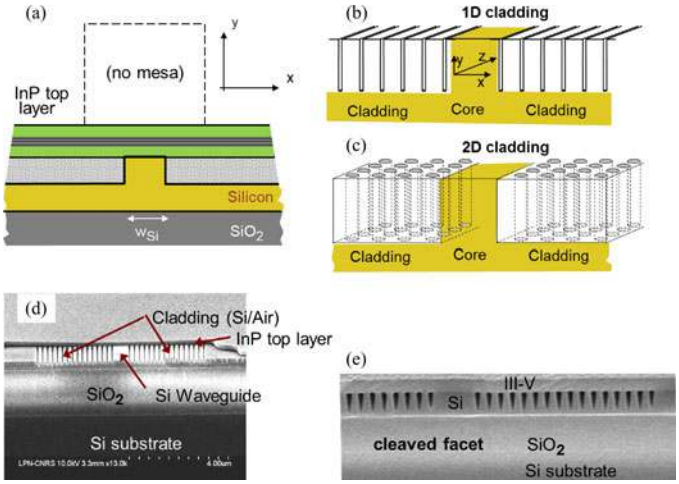

Fig. 1. (a) Scheme of the oxide-free directly bonded structure. The dotted area is an effective medium as shown in (b) for trenches or (c) for 2D PhC. (d) Micrograph intentionally taken at a partly delaminated cleaved edge to explain the structure, (e) typical mirror-like facet with materials indicated.

described in Fig. 1(a) and (b): it comprises a ridge of width w_{Si} typically spanning 600 to 1400 nm and two types of nanostructured cladding that extend on $\sim$3 μm around them, either trenches with typical air-filling factor $f \approx 0.30$ (period 200 nm, width 30 or 70 nm, depth $\sim$260 or $\sim$230 nm), or a square array of holes (period 180 nm, diameter $\sim$75 nm, depth 230 nm) with an area air-filling factor $f \approx 0.133$. These latter are photonic crystals (PhC) essentially used in the sub-wavelength regime below the photonic band gap. For the trenches, it was explained in [12] why a better confinement is expected for this trench direction aligned with the guide for a TE polarized mode.

On the InP side, we start from a MOVPE grown wafer with an InGaAs etch stop layer, followed by the stack to be bonded. It consists of a mere 400-nm-thick InP layer in the case of end-fire measurements, or a stack having 4 embedded InGaAs QWs (QW, with total well + barrier thicknesses of $\sim$ 80 nm) with two 70-nm-thick InP cladding. The QW peak PL lies at $\lambda \approx 1530$ nm. They are not intentionally strained, so TE and TM emission are available in the layer plane, with the latter slightly blue-shifted.

Oxide-free bonding takes place at $\sim$500 °C under vacuum, following the procedure described elsewhere [10] and for which we have checked that PL is nearly unaffected by this oxide-free direct bonding process by comparing it to the same layers bonded with other processes [11]. Also, the bonded layers are not delaminated upon chemo-mechanical polishing and cleavage.

Typical micrographs are shown in Fig. 1(c) and (d), after cleavage of the bonded pieces. Bonding works well on macroscopic areas ($>$1 mm^2), given that we bond quite small pieces (1 cm^2 SoI and $<$1 cm^2 InP). This allows defining 780-μm-wide cleaved bars that have waveguides terminated by straight facets.

III. ILS Measurements

We used a setup similar to that used for InP photonic crystal measurements [13], [14], with either a $\lambda = 675$ nm red laser excitation or a $\lambda = 980$ nm fibered laser diode excitation, better suited to vary the power in controlled manner. We collect both front PL and side PL after propagation in the waveguide. In our case, the waveguide ends at the facet.

One practical difficulty compared to earlier PhC measurements is that the guides are not much visible from the surface, being buried, depending on the kind of illumination used. Additional references have been patterned to find the waveguides location and their axis. We made cartographies of front PL to detect possible defects that would compromise the test of some waveguides.

Another difficulty is that PL is well preserved above the nanopatterned silicon lateral cladding (see Section VI), so there is no strong difference in front PL that helps assessing that excitation does take place well in the channel waveguide core. We also observed that even with excitation in the waveguide core, light is also generated in sizable amounts in the surrounding areas and then easily confined by the modest effective index difference between the cladding part (where, typically, $n_{\rm eff} \sim 3.0$) and the virgin parts ($n_{\rm eff} \sim 3.35$) because rays detected at the facet are those that propagate at grazing incidence with respect to the waveguide. Such behavior is by itself an assessment that the structure behaves much as a planar one with modulated effective index by the nanopattern, and with little scattering, which is our fundamental scope. Bubbles between Si and InP or other random delamination would cause detectable scattering that we did not observe. Especially, we did not observe any such effect in the nanopatterned area, so that the overall trend at this stage seems to be that nanopatterning is fully compatible with oxide-free direct bonding. This thus validates its potential to participate into new laser designs of interest for thermal and electrical purposes.

The more critical measurements concern the extinction of guided light into our nanopatterned waveguides. Our initial scope was to track the trends of the modal behavior through the variation of confinement factor induced by the variable ridge with : in a full laser design with a thick mesa on top of the InP side, squeezing the Si ridge causes the mode profile to migrate towards the InP multi-quantum wells (MQW) and thus increases the relevant confinement factor $\Gamma_{\rm MQW}$ in this area, and the correlative expected re-absorption, that our experiment is well suited to measure [15]. However, for the present bonded stack, the upper InP cladding layer is limited to 70 nm versus >1 μm for the simulated structures of [12], the mode distribution cannot migrate upward, and $\Gamma_{\rm MQW}$ loses most of its dependence on ridge width.

In this experiment, we indeed expect extinction both from absorption and from scattering by the nanopatterned cladding. From the spectral dependence of reabsorption, which can be assessed by measurement in nonpatterned parts, we can deduce the specific contribution of the scattering, within experimental uncertainties.

In practice, we measure spectra for PL excitation at four distances from the cleaved edge, $d = 100$, 150, 200 and 250 μm here, and we measure on the side both the TE and the TM polarized spectrum, while recording as well the front PL spectrum for normalization purpose.

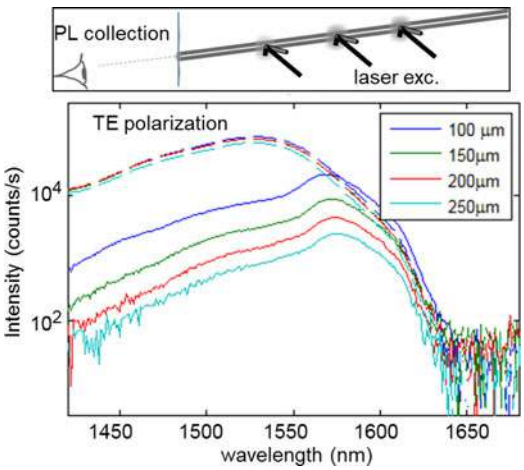

Fig. 2. Raw side PL spectra from the waveguide at increasing distances as indicated, for TE polarization (solid lines). The dashed lines are the front PL spectra, used for normalization purpose. The top inset describes the measurement geometry.

We thus expect the signal $I_1\,(d,\lambda)$ to be of the form

$$I_1\,(d,\lambda) = I_o\,\exp\left[-\left\{\alpha^{\rm pol}_{\rm MQW}\,(\lambda)+\alpha^{\rm pol}_{\rm SCATT}\,(\lambda)\right\}d\right] \quad (1)$$

where pol is TE or TM, and I_o is the intensity launched by local PL in the waveguide. If we perform an experiment outside waveguides in a virgin area, the trend is slightly different as there is a cylindrical divergence of the beam [16]:

$$I_1\,(d,\lambda) = \left(\frac{K}{d}\right)\exp\left[-\left\{\alpha^{\rm pol}_{\rm FREE}\,(\lambda)\right\}d\right]. \quad (2)$$

Scattering is expected to be different, in that case, it should stem only from interfaces with air and silica, and negligibly from the InP–Si interface since the sample appears as locally uniform from microscope inspection.

By inverting the appropriate equation, we can get the absorption or extinction of interest, $\alpha^{\rm pol}_{\rm FREE}\,(\lambda)$ and $\alpha^{\rm pol}_{\rm MQW}\,(\lambda)+\alpha^{\rm pol}_{\rm SCATT}\,(\lambda)$. If the modal distribution in the ridge case has an overlap $\Gamma_{\rm MQW}$ of the MQWs similar to that outside the waveguide, we can identify $\alpha^{\rm pol}_{\rm FREE}\,(\lambda)\approx\alpha^{\rm pol}_{\rm MQW}\,(\lambda)$. And then by difference, we can deduce the excess scattering losses that is mostly expected to stem from the overlap with the cladding area.

We present in Fig. 2 the raw waveguide spectra on semilog scale as solid lines, compared to the front PL (dashed curve). These data suggest that the guide is quite regular over its length as the curve smoothly evolves between the different probed positions.

The absorption deduced from similar TE and TM data taken first on non-patterned area, and to which Eq. (2) is applied, are shown in Fig. 3. In spite of some scatter in data, the typical absorption features of such QWs are well recognized. The alignment of the curves is reasonable. If some part of the waveguide were not truly bonded due to an air gap, the absorption would differ notably due to the change in confinement factor of the guided mode. Even for the less sensitive TE mode, an air gap of 50 nm between Si and InP would cause $\Gamma_{\rm MQW}$ and thus the

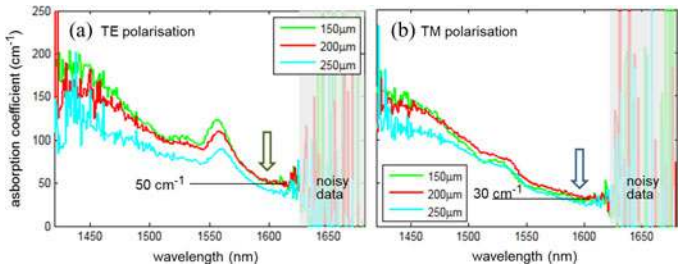

Fig. 3. (a) Absorption coefficient of un patterned area in TE and (b) in TM polarization.

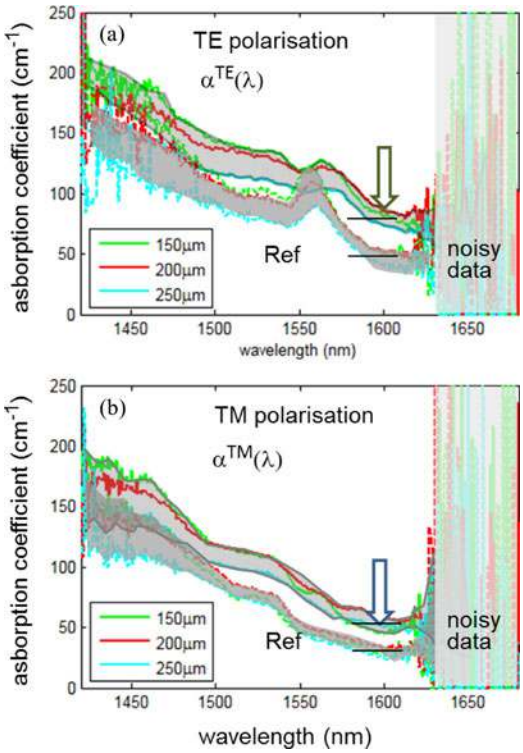

Fig. 4. (a) absorption for TE polarization in the channel waveguide (top three solid curves, underlined by a light gray shade) compared to non guiding area denoted "Ref" (bottom three dashed curves, shadowed by a light grey shade, data of Fig.3). (b) Same type of data for TM polarization.

absorption to decrease by over a factor of two, and even more for the TM case.

We now consider the measurements of a typical waveguide, as illustrated in Fig. 4. It is a waveguide clad with trenches having a 190 nm pitch, and with a $w_{\rm Si}=0.8$-μm-wide silicon ridge.

We see that there is a fairly constant excess extinction, even in the spectral region of the absorption tail of the MQW around $\lambda=1600$ nm. The only important change relates to the less pronounced feature of the quantum well excitonic-like absorption peak at 1560 nm. It is a somewhat surprising change, that has no plausible origin in the near-field effects (MQWs close to nanostructures, but not so close for the ridge part where most absorption takes place) and needs further assessment.

The excess losses that we can thus attribute with these measurements to scattering by the nanostructured cladding are given

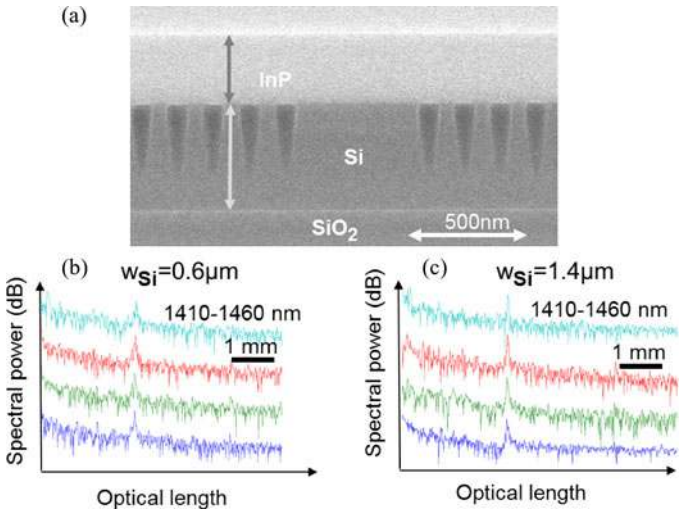

Fig. 5. InP membrane bonded on a PhC Si waveguide on SOI. (a) micrograph of a cleaved facet, (b) Fourier transform of the transmission spectra on 4 spectral 50-nm-wide windows for a $w_{Si} = 0.6$-μm-wide bonded waveguide [1410–1460, 1460–1510, 1510–1560, 1560–1610 nm from top to bottom], (c) same for a $w_{Si} = 1.4$-μm-wide waveguide.

by the distance between the two sets of curves. We thus find about 30 cm^{-1} for the TE polarization and 20 cm^{-1} for the TM polarization. These are rather large values and we think that these are upper bounds of the actual cladding-induced losses. Notably, there is a fair amount of light next to the waveguide in the current sample geometry, due to light leaking through the nanostructured area laterally, but being reflected by adjacent guides and contributing to total light at the cleaved facet in sizable proportion. It is delicate to give an exact estimate because the multimode collection fiber in the system cannot be related to precise imaging pixels, so the length of cleaved edge light not stemming from channel waveguides might become a sizable perturbation.

However, the main advantage of this method is the capability to probe many samples without difficult alignment and fast enough, say a few minutes per waveguide. Measurements on other waveguides have yielded figures which do not differ much from the exemplified one. More work is needed with this method to extract trends about the differences between the four kinds of cladding implemented and measured, and between the different ridge widths (that is used as the main parameter in the design study [12]). The presence of a mesa and some other photonic tricks could make the next measurements more fully relevant to the design issues that we initially tackled in [12].

IV. End-Fire Measurement

In parallel to the above data, a more traditional end-fire measurement of the waveguides was undertaken. In this case, a 400-nm-thick InP layer without anything else is bonded on the SOI waveguides, the Si guiding layer being 550 nm [see Fig. 5(a)], thus thicker. Waveguides with widths w_{Si} ranging from 0.6 μm to 1.4 μm including 20 rows of holes, diameter 50 nm period 150 nm on both sides have been measured.

The transmission measurement method is the same as implemented for various guiding systems, e.g., suspended tethered nanowires of photonic crystals [17]. The optical power of polarization-controlled tunable sources ($\lambda = 1410$–1610 nm) is launched through a polarization-maintaining lensed fiber and collected by a lensed fiber. We focus on the sole TE polarization that is usually of more interest for lasers or active devices. The waveguide length between the two cleaved facets was 780 μm.

We analyzed the transmitted Fabry–Perot fringes due to the two-cleaved facet reflections by taking the Fourier transform of four successive slices of the spectrum. Fig. 5(b) shows these Fourier transform signals in the case of a narrow $w_{Si} = 0.6$ μm waveguide, while Fig. 5(c) corresponds to the case of a $w_{Si} = 1.4$ μm wide waveguide. Both exhibit a single peak in all the spectral domains, evidencing the monomode behavior of bonded nanopatterned waveguides. From a single waveguide length, assuming an amplitude reflectivity of the facets $r = 0.6$, the propagation losses can be retrieved. For $w_{Si} = 1.0$ μm, propagation losses of 21 cm^{-1} have been measured on non-bonded Si nanostructured waveguides, and reach 25 cm^{-1} for bonded nanostructured waveguides, indicating that the bonding interface does not contribute significantly to the propagation losses, mainly originating from the nanostructure technology.

The spectra used in this study have also been used previously to determine the nanopattern-dependent group index and its dispersion in these waveguides, based on the wavelength-dependent period of the Fabry–Perot fringes [18].

V. Discussion

It is seen that the absorption found is around 20 cm^{-1} for the whole domain. This result falls in the range inferred by ILS method, and is rather less by a modest fraction. Some adverse factors have been invoked above for the accuracy of the ILS method in the current samples. It might also be that the top interface is not identically smooth between both samples.

We still think that the difference between TE and TM is a genuine one, and that it can be used to confirm that the origin of the current losses lies in the nanopatterned cladding: we can relate scattering strength to the modal characteristics by assuming that the dominant field component normalized strength at the sidewalls and interfaces is the main determinant of the scattering strength. In wavelength-scale photonic crystals, the situation is complex due to the fact that the polarization perturbation induced by irregularities does not radiate the same way according to dipole orientation and thus local polarization direction. This is not so much the case here since the medium is subwavelength, so that a vertical or horizontal dipole can be expected to radiate a comparable amount in a waveguide whose total thickness of 630 nm is a bit too large to get large electrodynamics effects (unlike in, say, 350-nm square silicon rods).

Simulation of the fields made as in ref. [12] first confirms that, as a function of w_{Si}, the strength of the quasi-TE guided mode field at the vertical ridge side/effective material cladding interface gently saturates from $w_{Si} = 0.6$ μm on, while the strength of the guided mode at the Si/InP interface on the mesa ridge decays as the mode expands more in both InP and Si

for increasing w_{Si}, with an eventual w_{Si}^{-1} trend. Furthermore, it indicates that, at the ridge side/effective material interface, for $w_{Si} = 0.8$ μm, the strength of field D_x ($=\varepsilon E_x$) for the quasi-TE mode and of the field D_y for the quasi-TM mode, are in a 5:4 ratio. This ratio is compatible, within uncertainties, with the two modal loss values of 30 and 20 cm^{-1} found above by the ILS method, neglecting the complex physics of polarization-dependent scattering on account of the reduced index contrast for the nanopatterned cladding. It leaves room for a differential contribution $\sim$<5 cm^{-1} from the top interface.

VI. Band-Filling Studies

As a final capability of micro-PL measurements, we attempted to check how the optical properties of the nanopattern as well as its thermal conductance could be locally mapped using PL light as a probe. We start from the fact that when varying the PL excitation power $P_{\rm exc}$, there is some band-filling in the MQW. Denoting N its carrier density, in a bimolecular recombination limit, the recombination rate reads BN^2 ($B \equiv$ Einstein coefficient). It is balanced by a generation rate G scaling like $P_{\rm exc}$, thus leading to a $N \propto (P_{\rm exc})^{1/2}$ functional dependence easy to check graphically. Band-filling thus leads to a blue shift ($\Delta\lambda < 0$) of the PL spectrum, proportional to N. The shift determination $\Delta\lambda$ can be made extremely accurate (within $\sim$20 pm) by using the centroid of the spectrum raised to a small exponent, I(λ)^p with $p = 3$ for instance, a method from signal processing [19], [20].

Differences in the slope of $\Delta\lambda$ versus $(P_{\rm exc})^{1/2}$ then depend on the excitation efficiency, i.e., how the laser creates carriers in the MQW. The local power scales as the generation rate, thus as N^2 and finally as the square of the slope. This quantity deduced from PL spectra is thus immune to variations of PL extraction that are awkward to assess in structured samples. There are indeed large variations of excitation efficiency in our samples due to the reflection of the 980 nm exciting beam onto the various layers of the SOI + InP stack. A simple transfer matrix simulation easily provides the local squared electric field amplitude across the MQW location spanning 80 nm. The exact thickness of the $t_{\rm silica} = 1.56-\mu$m-thick buried oxide layer, matters and gives rise to quickly varying reflections, in spite of its modest order of interference (this thickness is about 5($\lambda/2n$) for $\lambda = 980$ nm and $n\sim$1.47 for silica). We shall thus present a calculation for $t_{\rm silica} = 1565 \pm 10$ nm.

As for the thermal differences, we observe that much as in lasers (e.g., tunable lasers, see [21]), the local heating induced by the locally dissipated power gives rise to a red shift of the PL peak, with the usual 0.5 nm/K slope for 1550 nm quaternaries. This thermal shift being proportional to the incident power, it translates into a *quadratic* red-shift-oriented trend in the plot of $\Delta\lambda$ versus $(P_{\rm exc})^{1/2}$, an upward curvature.

A last point is to ensure proper focusing when performing this experiment. Many of the band-filling probing done here at a constant focus were repeated by scanning the sample longitudinally along the optical axis, and by correcting the spectral-spatial map thus obtained for chromatic aberration, etc.; such a map offers a reproducible focus since a longitudinal scan shall pass through the very focus of the excitation beam, which is a setup characteristics. Overall, the conclusions were consistent with the simpler study of $\Delta\lambda$ versus $(P_{\rm exc})^{1/2}$ and, thus, we do not expand more on that.

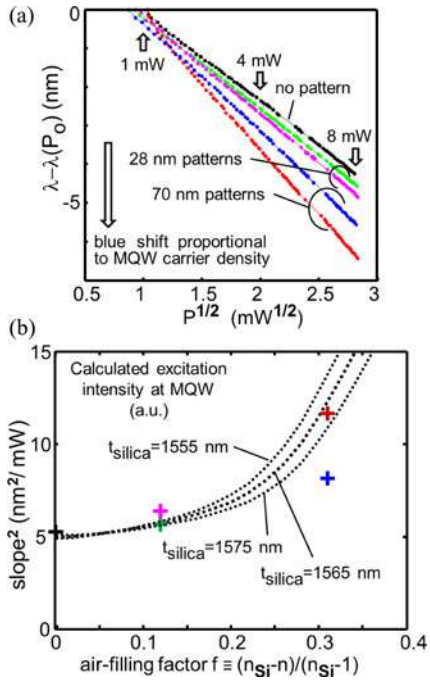

Fig. 6. (a) Blue shift of the PL peak as a function of the square root of exciting power for localized excitation either in a nonpatterned area or in patterned areas. The slopes and hence the MQW carrier densities differ. (b) Crosses : fitted slopes as a function of the air filling-factor of the underlying pattern ($f =$ 0, black cross, f = 0.127 and f = 0.3, coloured crosses); dotted lines: calculated local intensity (a.u.) averaged over MQW and set-up excitation angles, for three silica thicknesses, $t_{\rm silica} = 1565$ nm at 10 nm around.

We first compared III–V MQW stacks bonded on bulk silicon to the original stacks on their InP wafer. We found no sign of thermal drift, i.e. no detectable quadratic trend, at variance with the case of a stack bonded with $\sim$1 μm BCB on a silicon wafer. We did find in this case a noticeable quadratic upward bending, of $\Delta\lambda \sim +$ 1–2 nm over a total $\Delta\lambda \sim$ –8 nm blue shift for our typical 8 mW maximum power (small enough to remain nearly bimolecular). This observation suggests that a hidden delaminated bonding in a bonded stack, and its associated thermal resistance, would unavoidably appear with a similar trend, making a micro-PL scan a versatile probe.

We attempted to compare the blue-shift response for either non patterned areas, or for patterned area of one-dimensional nature. The results, Fig. 6 (a), exhibit a nice linear trend, with clearly more band-filling for the samples on patterns than for the samples on 100% silicon. In Fig. 6(b), we suggest that the local field in the MQW is the most likely reason for this trend. The dotted lines are transfer-matrix calculations of the local intensity at the MQW versus the degree of porosity (we actually vary the index, assuming an exciting field polarized along the grooves). The crosses are the squared slopes of Fig. 6(a). It can be seen that there is a reasonable degree of agreement, although the exact value of silica's optical path critically matters. Another point is the apparent absence of quadratic trend in Fig. 6(a), which suggests that the nanopatterned cladding behaves well thermally.

VII. Conclusion

To conclude these studies, we have characterized novel waveguides made from InP directly bonded to Si with a genuinely oxide-free process. Designs with nanostructured cladding in the silicon, suggested recently to improve thermal and electrical characteristics of hybrid lasers, have been implemented (with trenches in 1-D trenchand holes in 2-D) and measured in different waveguides and experimental setup: using MQW as an internal light source, or with end-fire injection. Band-filling studies by fine analysis of PL power dependent spectra were introduced for the purpose of gaining local knowledge on pattern and interfaces of embedded parts of the structure, as it is not possible for μm-scale nanopatterns to get data by traditional ellipsometry for instance.

From the collected data, an excess loss attributed to the nanostructured cladding was found to be typically 20 cm^{-1}. Further investigations are needed to understand what elements of the design and technology contribute to this sizable loss, but most probably the vertical sidewalls. On the positive side, no sign of hidden delamination along the waveguide path could be found. On the contrary, all aspects of measurements indicate that the nanostructured cladding do behave 1) as an effective material with high ordinary or extraordinary indices and 2) as a good thermal conductor. Therefore, there is a good hope that, exploiting the best of the highly developed silicon technology, hybrid lasers with good optical characteristics and improved performances can be elaborated from the oxide-free bonding strategy.

References

[1] A. W. Fang, H. Park, Y. H. Kuo, R. Jones, O. Cohen, D. Liang, O. Raday, M. N. Sysak, M. J. Paniccia, and J. E. Bowers, "Hybrid silicon evanescent devices," *Mater. Today*, vol. 10, pp. 28–35, 2007.

[2] G. Roelkens, L. Liu, D. Liang, R. Jones, A. Fang, B. Koch, and J. Bowers, "III–V/silicon photonics for on-chip and intra-chip optical interconnects," vol. 4, p. 779, 2010.

[3] S. Srinivasan, A. W. Fang, D. Liang, J. Peters, K. Bryan, and J. E. Bowers, "Design of phase-shifted hybrid silicon distributed feedback lasers," *Opt. Exp.*, vol. 19, pp. 9255–9261, 2011.

[4] K. Tanabe, K. Watanabe, and Y. Arakawa, "III–V/Si hybrid photonic devices by direct fusion bonding," *Sci. Rep.*, vol. 2, 2012.

[5] G. Roelkens, J. Van Campenhout, J. Brouckaert, D. Van Thourhout, R. Baets, P. Rojo-Romeo, P. Regreny, A. Kazmierczak, C. Seassal, X. Letartre, G. Hollinger, J. M. Fedeli, L. Di Cioccio, and C. Lagahe-Blanchardd, "III-V/Si photonics by die-to-wafer bonding," *Mater. Today*, vol. 10, pp. 36–43, 2007.

[6] S. Stankovic, R. Jones, M. N. Sysak, J. M. Heck, G. Roelkens, and D. Van Thourhout, "1310-nm hybrid III-V/Si fabry-pérot laser based on adhesive bonding," *IEEE Photon. Technol. Lett.*, vol. 23, no. 23, pp. 1781–1783, Dec. 2011.

[7] M. Lamponi, S. Messaoudene, S. Keyvaninia, C. Jany, F. Poingt, F. Lelarge, G. De Valicourt, G. Roelkens, D. Van Thourhout, J. Fedeli, and G. H. Duan, "Low-threshold heterogeneously integrated InP/SOI lasers with a double adiabatic taper coupler," *IEEE Photon. Technol. Lett.*, vol. 24, no. 1, pp. 76–78, Jan. 2012.

[8] J. Van Campenhout, P. Rojo Romeo, P. Regreny, C. Seassal, D. Van Thourhout, S. Verstuyft, L. Di Cioccio, J. M. Fedeli, C. Lagahe, and R. Baets, "Electrically pumped InP-based microdisk lasers integrated with a nanophotonic silicon-on-insulator waveguide circuit," *Opt. Exp.*, vol. 15, pp. 6744–6749, 2007.

[9] K. Tanabe, K. Watanabe, and Y. Arakawa, "1.3 μm InAs/GaAs quantum dot lasers on Si rib structures with current injection across direct-bonded GaAs/Si heterointerfaces," *Opt. Exp.*, vol. 20, p. B315-B321, 2012.

[10] A. Talneau, C. Roblin, A. Itawi, O. Mauguin, L. Largeau, I. Sagnes, and G. Patriarche, "Atomic-plane-thick reconstruction across the interface during heteroepitaxial bonding of InP-clad quantum wells to Si," presented at the Inst. Planning Resource Manage., Santa Barbara, CA, USA, 2012.

[11] A. Talneau, C. Roblin, A. Itawi, O. Mauguin, L. Largeau, G. Beaudoin, I. Sagnes, G. Patriarche, C. Pang, and H. Benisty, "Atomic-plane-thick reconstruction across the interface during heteroepitaxial bonding of InP-clad quantum wells on Silicon," *Appl. Phys. Lett.*, vol. 102, pp. 212101–212103, 2013.

[12] C. Pang and H. Benisty, "Nanostructured silicon geometries for directly bonded hybrid III–V-silicon active devices," *Photon. Nanostruct.-Fundamentals Appl.*, vol. 11, pp. 145–156, 2013.

[13] S. Olivier, H. Benisty, C. Weisbuch, C. J. M. Smith, T. F. Krauss, R. Houdré, and U. Oesterle, "Improved 60° bend transmission of submicron-width waveguides defined by two-dimensional photonic crystals," *IEEE J. Lightw. Technol.*, vol. 20, no. 7, pp. 1198–1203, Jul. 2002.

[14] H. Benisty, S. Olivier, C. Weisbuch, M. Agio, M. Kafesaki, C. M. Soukoulis, M. Qiu, M. Swillo, A. Karlsson, B. Jaskorzynska, A. Talneau, J. Moosburger, M. Kamp, A. Forchel, R. Ferrini, R. Houdré, and U. Oesterle, "Models and measurements for the transmission of submicron-width waveguide bends defined in two-dimensional photonic crystals," *IEEE J. Quantum Electron.*, vol. 38, no. 7, pp. 770–785, Jul. 2002.

[15] E. Schwoob, H. Benisty, C. Weisbuch, C. Cuisin, E. Derouin, O. Drisse, G.-H. Duan, L. Legouézigou, E. Legouézigou, and F. Pommereau, "Enhanced gain measurement at mode singularities in InP-based photonic crystal waveguides," *Opt. Exp.*, vol. 12, pp. 1569–1574, 2004.

[16] D. Labilloy, H. Benisty, C. Weisbuch, T. F. Krauss, D. Cassagne, C. Jouanin, R. Houdré, U. Oesterle, and V. Bardinal, "Diffraction efficiency and guided light control by two-dimensional photonic-band-gap lattices," *IEEE J. Quantum Electron.*, vol. 35, no. 7, pp. 1045–1052, Jul. 1999.

[17] A. Talneau, K. H. Lee, S. Guilet, and I. Sagnes, "Efficient coupling to W1 photonic crystal waveguide on InP membrane through suspended access guides," *Appl. Phys. Lett.*, vol. 92, pp. 061105–061103, 2008.

[18] X. Pommarede, A. Talneau, C. Pang, and H. Benisty, "Modal engineering and experimental characterization of InP bonded on SOI photonic crystal waveguides implementing effective medium theory," private communication.

[19] S.-H. Baik, S.-K. Park, C.-J. Kim, and B. Cha, "A center detection algorithm for Shack–Hartmann wavefront sensor," *Opt. Laser Technol.*, vol. 39, pp. 262–267, 2007.

[20] K. Bougot-Robin, W. Wen, and H. Benisty, "Resonant waveguide sensing made robust by onchip peak tracking through image correlation," *Biomed. Opt. Exp.*, vol. 3, pp. 2436–2451, 2012.

[21] S. Mahnkopf, R. März, M. Kamp, G. H. Duan, F. Lelarge, and A. Forchel, "Tunable photonic crystal coupled-cavity laser," *IEEE J. Quantum Electron.*, vol. 40, no. 9, pp. 1306–1314, Sep. 2004.